

# Topological defects of spin-orbit coupled Bose-Einstein condensates in a rotating anharmonic trap

Chunxiao Shi<sup>1</sup>, Linghua Wen<sup>1,2,\*</sup>, Qingbo Wang<sup>1,3</sup>, Hui Yang<sup>1,4</sup>, and Huan Wang<sup>1</sup>

<sup>1</sup>Key Laboratory for Microstructural Material Physics of Hebei Province, School of Science, Yanshan University, Qinhuangdao 066004, China

<sup>2</sup>Department of Physics and Astronomy, University of Pittsburgh, Pittsburgh, Pennsylvania 15260, USA

<sup>3</sup>Department of Physics, Tangshan Normal University, Tangshan 063000, China

<sup>4</sup>Department of Physics, Xinzhou Teachers University, Xinzhou 034000, China

We investigate the topological defects and spin structures of binary Bose-Einstein condensates (BECs) with Dresselhaus spin-orbit coupling (D-SOC) in a rotating anharmonic trap. Our results show that for initially mixed BECs without SOC the increasing rotation frequency can lead to the structural phase transition of the system. In the presence of isotropic D-SOC, the system sustains vortex pair, Anderson–Toulouse coreless vortices, circular vortex sheets, and combined vortex structures. In particular, when the rotation frequency is fixed above the radial trapping frequency the strong D-SOC results in a peculiar topological structure which is comprised of multi-layer visible vortex necklaces, hidden vortex necklaces and a hidden giant vortex. In addition, the system exhibits rich spin textures including basic skyrmion, meron cluster, skyrmion string and various skyrmion lattices. The skyrmions will be destroyed in the limit of large D-SOC or rotation frequency. Furthermore, the effects of anisotropic D-SOC and Rashba-Dresselhaus SOC on the topological structures of the system are discussed.

## 1. Introduction

One of the most exciting recent developments in cold atom physics has been the production of spin-orbit-coupled quantum gases.<sup>1–4</sup> The spin-orbit coupling (SOC) between a quantum particle’s spin and its momentum in solid materials is essentially an intrinsic property of the materials and can not be controlled due to the unavoidable impurities and disorder.<sup>5,6</sup> By contrast, the SOC in neutral atomic gases can be controlled effectively through a series of experimental parameters,<sup>1–4,7–9</sup> which means that the ultra-cold atomic gases with SOC provide an ideal platform to explore the novel quantum states and relevant dynamics.<sup>10–25</sup> Typically, the nonrotating spin-orbit coupled Bose-Einstein condensates (BECs) in a harmonic trap support plane-wave phase,<sup>15</sup> stripe phase,<sup>9,10,15</sup> half-quantum vortex,<sup>11–13</sup> bright soliton,<sup>21,26,27</sup> dark soliton,<sup>28,29</sup> gap soliton,<sup>30</sup> and topological superfluid phase.<sup>4</sup> In particular, the combination effect of SOC and rotation on BECs has been shown to be able to create various topological defects. These intriguing results enrich the phase diagram and physics of condensate system. To the best of our knowledge, however, most literature concerning on the rotating spin-orbit coupled BECs focuses on the harmonic trap.<sup>31–36</sup> In the case of rotating harmonic trap, the rotation angular frequency  $\Omega$  is generally limited to a relatively small value far below the radial trapping frequency  $\omega_{\perp}$ . In the limit  $\Omega/\omega_{\perp} \rightarrow 1$ , a rotating BEC is expected to undergo complicated quantum phase transition from superfluid to various highly correlated ground states (nonsuperfluid states). Indeed, this situation is singular because the total angular momentum and the Thomas-Fermi (TF) radius of the BEC both diverge.

In actual experiments, the trap usually is not purely harmonic. With this concern, we study the ground-state structures of spin-orbit coupled BECs in a rotating anharmonic trap (a rotating harmonic trap with a quartic distortion).<sup>37</sup> Such

an anharmonic trap can confine the BECs even for  $\Omega/\omega_{\perp} > 1$ , and therefore allowing a more controlled investigation of possible new states which are not generally the same as those expected in a harmonic trap. For the spin-orbit interaction, here we mainly consider the Dresselhaus SOC (D-SOC) and Rashba-Dresselhaus SOC (RD-SOC) which can be realized under current experimental conditions.<sup>1–4,7–9,19,38,39</sup> For initially mixed two-component BECs without SOC, we show that structural change of vortex patterns can be achieved by regulating the rotation frequency. In the presence of SOC, the system can exhibit rich vortex defects and various kinds of skyrmion structures.<sup>40–42</sup> Particularly, for the case of large D-SOC strength or rotation frequency, the skyrmion structures will be destroyed due to the overlap between the two components. In addition, the combined effects of SOC, rotation, interatomic interactions and anharmonic trap are revealed and discussed. Furthermore, we find that there are evident differences for the vortex structures and spin textures between the rotating BECs with D-SOC and those with RD-SOC.

The paper is organized as follows. In section 2, the theoretical model is introduced and the coupled dynamic equations are given. The topological structures and relevant spin textures of the system are presented and analyzed in section 3. Our findings are summarized in the last section.

## 2. Model

By assuming tight confinement in the  $z$  direction, we consider a quasi-two-dimensional system of rotating two-component BECs with D-SOC which are confined in an anharmonic trap (i.e., a harmonic plus quartic trap). The energy functional of the system is given by

$$E = \int \sum_{j=1,2} \left\{ -\frac{\hbar^2}{2m} |\nabla\psi_j|^2 + V_{tr}(r) |\psi_j|^2 + \frac{g_j}{2} |\psi_j|^4 \right.$$

\*linghuawen@ysu.edu.cn

$$\begin{aligned}
& + \hbar \psi_j^* \left[ -i \lambda_x \frac{\partial \psi_{3-j}}{\partial x} + (-1)^j \lambda_y \frac{\partial \psi_{3-j}}{\partial y} \right] - \Omega \psi_j^* L_z \psi_j \Big\} d^2r \\
& + \int g_{12} |\psi_1|^2 |\psi_2|^2 d^2r, \quad (1)
\end{aligned}$$

where  $\psi_{1,2}$  denote the two-component (i.e., spin-up and spin-down) wave functions, and they are normalized as  $\int [|\psi_1|^2 + |\psi_2|^2] dx dy = N$  with  $N$  being the total particle number.  $g_j = 4\pi a_j \hbar^2 / m$  ( $j = 1, 2$ ) and  $g_{12} = 2\pi a_{12} \hbar^2 / m$  denote the intra- and intercomponent interaction strengths that are characterized by the corresponding  $s$ -wave scattering lengths  $a_j$  and  $a_{12}$  between intra- and interspecies atoms and the atomic mass  $m$ .  $\Omega$  is the rotation frequency along the  $z$  direction, and  $L_z = i\hbar(y\partial_x - x\partial_y)$  denotes the  $z$  component of the angular-momentum operator. The D-SOC is written as  $v_D = i\hbar(\lambda_x \sigma_y \partial_x + \lambda_y \sigma_x \partial_y)$ ,<sup>1</sup> where  $\sigma_{x,y}$  are the Pauli matrices and  $\lambda_x$  and  $\lambda_y$  are the SOC strengths in the  $x$  and  $y$  directions. The anharmonic trap  $V_{tr}(r)$ <sup>37</sup>) is described by

$$V_{tr}(r) = \frac{1}{2} m \omega_{\perp}^2 \left( r^2 + \mu \frac{r^4}{a_0^2} \right) = \frac{1}{2} \hbar \omega_{\perp} \left( \frac{r^2}{a_0^2} + \mu \frac{r^4}{a_0^4} \right), \quad (2)$$

with  $\omega_{\perp}$  being the radial trap frequency and  $a_0 = \sqrt{\hbar/m\omega_{\perp}}$  being the harmonic-oscillator length. Here  $r = \sqrt{x^2 + y^2}$  is the radial coordinate in two-dimensions, and  $\mu$  is a dimensionless constant that characterizes the anharmonicity of the trap. For the sake of numerical calculation, it is convenient to introduce the following notations  $\tilde{r} = r/a_0$ ,  $\tilde{t} = \omega_{\perp} t$ ,  $\tilde{V}_{tr}(r) = V_{tr}(r)/\hbar\omega_{\perp} = (\tilde{r}^2 + \mu\tilde{r}^4)/2$ ,  $\tilde{\Omega} = \Omega/\omega_{\perp}$ ,  $\tilde{L}_z = L_z/\hbar$ , and  $\tilde{\psi}_j = \psi_j a_0 / \sqrt{N}$  ( $j = 1, 2$ ). Then we obtain the dimensionless coupled Gross-Pitaevskii (GP) equations in the rotating frame by using a variational method,

$$\begin{aligned}
i\partial_{\tilde{t}}\psi_1 &= \left( -\frac{1}{2}\nabla^2 + V_{tr} + \beta_{11} |\psi_1|^2 + \beta_{12} |\psi_2|^2 - \Omega L_z \right) \psi_1 \\
&+ (\lambda_x \partial_x + i\lambda_y \partial_y) \psi_2, \quad (3)
\end{aligned}$$

$$\begin{aligned}
i\partial_{\tilde{t}}\psi_2 &= \left( -\frac{1}{2}\nabla^2 + V_{tr} + \beta_{22} |\psi_2|^2 + \beta_{12} |\psi_1|^2 - \Omega L_z \right) \psi_2 \\
&+ (-\lambda_x \partial_x + i\lambda_y \partial_y) \psi_1, \quad (4)
\end{aligned}$$

where the tilde is omitted for simplicity. Here  $\beta_{jj}$  ( $j = 1, 2$ ) and  $\beta_{12} = \beta_{21}$  are the dimensionless intra- and interspecies coupling strengths. In section 3 of the paper, we will also demonstrate the effect of RD-SOC  $v_{RD} = -i\hbar(\lambda_x \sigma_x \partial_x + \lambda_y \sigma_y \partial_y)$ <sup>43,44</sup>) on the ground state of the system, where the dimensionless dynamic equations with RD-SOC are expressed by

$$\begin{aligned}
i\partial_{\tilde{t}}\psi_1 &= \left( -\frac{1}{2}\nabla^2 + V_{tr} + \beta_{11} |\psi_1|^2 + \beta_{12} |\psi_2|^2 - \Omega L_z \right) \psi_1 \\
&+ (-i\lambda_x \partial_x - \lambda_y \partial_y) \psi_2, \quad (5)
\end{aligned}$$

$$\begin{aligned}
i\partial_{\tilde{t}}\psi_2 &= \left( -\frac{1}{2}\nabla^2 + V_{tr} + \beta_{22} |\psi_2|^2 + \beta_{12} |\psi_1|^2 - \Omega L_z \right) \psi_2 \\
&+ (-i\lambda_x \partial_x + \lambda_y \partial_y) \psi_1. \quad (6)
\end{aligned}$$

By using the nonlinear Sigma model, we introduce a normalized complex-valued spinor  $\chi = [\chi_1, \chi_2]^T$  with the normalization condition  $|\chi_1|^2 + |\chi_2|^2 = 1$ . The corresponding component wave function is  $\psi_j = \sqrt{\rho} \chi_j$  ( $j = 1, 2$ ) and the total density is  $\rho = |\psi_1|^2 + |\psi_2|^2$ . The spin density is given by  $\mathbf{S} = \bar{\chi} \boldsymbol{\sigma} \chi$ , where  $\boldsymbol{\sigma} = (\sigma_x, \sigma_y, \sigma_z)$  are the Pauli matrices. The components of  $\mathbf{S}$

can be written as

$$S_x = \frac{1}{\rho} (\psi_1^* \psi_2 + \psi_2^* \psi_1), \quad (7)$$

$$S_y = \frac{-i}{\rho} (\psi_1^* \psi_2 - \psi_2^* \psi_1), \quad (8)$$

$$S_z = \frac{1}{\rho} (|\psi_1|^2 - |\psi_2|^2), \quad (9)$$

where the norm of the spin is  $|\mathbf{S}| = \sqrt{S_x^2 + S_y^2 + S_z^2} = 1$ . In terms of the above expressions, we show that the different density distributions of the ground state lead to different spin density profiles, i.e., different spin textures carrying with different topological charges. The spatial distribution of topological structure of the system can be well described by the topological charge density

$$q(\mathbf{r}) = \frac{1}{4\pi} \mathbf{S} \bullet \left( \frac{\partial \mathbf{S}}{\partial x} \times \frac{\partial \mathbf{S}}{\partial y} \right), \quad (10)$$

and the topological charge is defined as  $Q = \int q(\mathbf{r}) dx dy$ . Furthermore, the total topological charge  $|Q|$  is conserved if one exchanges  $S_x$ ,  $S_y$ , and  $S_z$ .

### 3. Results and discussion

In order to study the ground-state structures of the system and the corresponding spin textures, we numerically calculate the two-dimensional (2D) coupled GP Equations (3)-(6) in terms of the imaginary-time propagation method<sup>46-48</sup>) based on the split-step Fourier method.<sup>15</sup>) Recently, phase diagrams for a BEC with Rashba SOC (R-SOC) in a nonrotating harmonic trap and in a rotating one have been given in Ref.<sup>34</sup>) In the present work, we systematically investigate the combined effects of rotation, SOC and interatomic interactions on the ground states of the BECs in an anharmonic trap. In our simulation, we assume the intra- and interspecies interactions to be repulsive. Without loss of generality, the anharmonicity parameter of the external trap is chosen as  $\mu = 1/2$ , and the intra-component interaction strengths are fixed as  $\beta_{11} = \beta_{22} = 200$ . For convenience, we introduce a relative interaction strength,  $\delta = \beta_{12}/\beta_{11}$ , where the initial state corresponds to an immiscible state when  $\delta > 1$  (initially immiscible), while it corresponds to a miscible state when  $\delta < 1$  (initially miscible). It is shown that system can exhibit intriguing properties which are inaccessible in other systems.

#### 3.1 Effect of rotation in the absence of SOC

In Fig. 1 we show the density profiles (the first two rows) and the corresponding phase profiles (the middle two rows) for the ground states of spin-1/2 BECs in a rotating anharmonic trap, and the last row represents  $|\psi_1|^2 + |\psi_2|^2$ . Here  $\delta = 0.5$ ,  $\lambda_x = \lambda_y = 0$ , and the rotation frequencies in columns (a)-(d) are  $\Omega = 0.5$ ,  $\Omega = 1.65$ ,  $\Omega = 1.7$  and  $\Omega = 3.0$ , respectively. For relatively small rotation frequency  $\Omega = 0.5$ , a singly quantized vortex occurs spontaneously in each component (see Fig. 1(a)). The system begins to exhibit partial phase separation in spite of the two components being mixed initially, which is caused by the competition among the total interaction energy, the kinetic energy (especially for the rotational kinetic energy) and the anharmonic external potential.<sup>46</sup>) When  $\Omega = 1.65$ , stable square vortex lattice forms in

each component, where the vortices in the two components are spatially staggered due to the repulsive interspecies interaction. As rotation frequency increases, the number of visible vortices gradually increases and the square vortex lattice evolves into a triangular vortex lattice (see Fig. 1(c)). This property is nontrivial as it has not been reported before. According to previous literature,<sup>49,50</sup> only the structural phase transition from triangular vortex lattice to square vortex lattice can possibly occur in two-component BECs in a rotating harmonic trap. Our numerical simulation shows that the trend of the structural phase transition is irrelevant to the relative interaction strength  $\delta$ . The main reason for this difference is the presence of anharmonic trap which makes the regimes of ultrafast rotation  $\Omega > 1$  and new phenomena become accessible. With the further increase of rotation frequency, e.g.,  $\Omega = 3$ , we can find that the visible vortices form a vortex necklace, where the vortices are distributed along a ring. In particular, as displayed in Fig. 1(d), hidden vortices<sup>51–54</sup> show up in the central region of the atom cloud and they form a hidden giant vortex plus a hidden vortex necklace (i.e., an annular hidden vortex lattice), which is remarkably different from the topological structures of the BECs in a rotating harmonic potential.<sup>31–34,49,50</sup> In the latter case, the central density hole is a simple giant vortex.

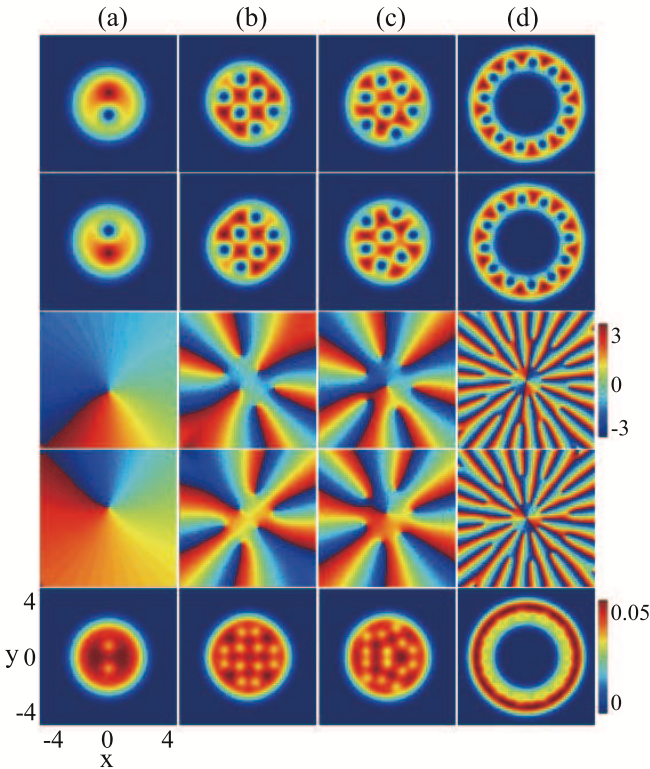


**Fig. 1.** (Color online) Ground states of interacting spin-1/2 BECs without SOC in a rotating anharmonic trap, where  $\lambda_x = \lambda_y = 0$  and  $\delta = 0.5$ . (a)  $\Omega = 0.5$ , (b)  $\Omega = 1.65$ , (c)  $\Omega = 1.7$ , and (d)  $\Omega = 3$ . The rows from top to bottom represent  $|\psi_1|^2$ ,  $|\psi_2|^2$ ,  $\arg \psi_1$ ,  $\arg \psi_2$  and  $|\psi_1|^2 + |\psi_2|^2$ , respectively. The horizontal and vertical coordinates  $x$  and  $y$  are in units of  $a_0$ .

Besides the line-like vortex excitation with respect to the spatial degrees of freedom of the BECs, the spin degrees of freedom allow for point-like topological excitation (skyrmion excitation) whose structure and topology are fixed by sim-

ple energy stability. Although skyrmions are already known in nuclear physics,<sup>40</sup> quantum Hall systems,<sup>55</sup> and liquid crystals,<sup>56</sup> generating these topological excitations in ultracold atomic gases would provide a new opportunity for understanding their physical properties in much greater detail. In addition, the skyrmion excitations in the ultracold atomic gases enable a thorough comparison between the experiments and relevant theories due to the ultrahigh purity and precise controllability of the cold-atom system. Obviously, the skyrmion excitations do not have an analogy in a scalar BEC. Shown in Figs. 2(a) and 2(b) are the topological charge density and the spin texture for the parameters in Fig. 1(b). The local enlargement of the spin texture is given in Figs. 2(c) and 2(d). In Figs. 2(e) and 2(f) we display the spin texture and the local enlargement for the parameters in Fig. 1(d), respectively. The color of each arrow in the spin textures indicates the magnitude of  $S_z$ . According to Ref.,<sup>41</sup> there are seven basic types of skyrmions in BECs in view of the skyrmion solution with  $|S|^2 = 1$ : radial-out skyrmion, radial-in skyrmion, circular skyrmion, hyperbolic skyrmion, hyperbolic-radial(out) skyrmion, hyperbolic-radial(in) skyrmion and circular-hyperbolic skyrmion. From Fig. 2(b) we can see that there are a series of circular-hyperbolic skyrmions (Fig. 2(c)) and hyperbolic-radial(out) skyrmions (Fig. 2(d))<sup>41</sup> which collectively constitute a composite skyrmion lattice. For the larger rotation frequency  $\Omega = 3$ , the spin texture becomes more complex and the skyrmions form two concentric annular skyrmion lattices as shown in Fig. 2(e), where the skyrmion configurations include multiple basic types.<sup>41</sup> The local circular-hyperbolic skyrmion in Fig. 2(f) is similar to that in Fig. 2(c) except for the opposite circular spin current direction. Our calculation shows that the topological charge of each skyrmion is  $|Q| = 1$ , which is consistent with the definition.<sup>40–42</sup>

In general, Dzyaloshinskii-Moriya interaction plays a key role in the formation of magnetic skyrmions in chiral magnets, which is induced by the relativistic spin-orbit coupling.<sup>57,58</sup> The typical skyrmions in magnetic materials are Bloch-type skyrmion, Néel-type skyrmion, and intermediate-type skyrmion.<sup>59,60</sup> However, the skyrmions in trapped BECs are expected to display more novel properties and richer structures due to the precise controllability of many experimental parameters of ultracold atoms. Essentially, the skyrmions in the spin textures of the two-component BECs are associated with the vortices in the component density distributions, and the particle density must satisfy the continuity condition as a result of quantum fluid nature of the BECs. Our simulation shows that the skyrmions in BECs are jointly determined by multiple parameters such as interatomic interactions, rotation frequency, SOC, and external potential. In contrast to magnetic materials, SOC is not a necessary condition for the formation of skyrmions in multi-component BECs. For rotating two-component BECs without SOC, one can define three new coupling constants:  $c_0 = (\beta_{11} + \beta_{22} + 2\beta_{12})/4$ ,  $c_1 = (\beta_{11} - \beta_{22})/2$ , and  $c_2 = (\beta_{11} + \beta_{22} - 2\beta_{12})/4$ .<sup>45,61</sup> The coefficient  $c_1$  may be regarded as a longitudinal (pseudo) magnetic field that aligns the spin along the  $z$  axis. The coefficient  $c_2$  describes the spin-spin interaction associated with  $S_z$ , where the system is ferromagnetic for  $c_2 < 0$  and antiferromagnetic for  $c_2 > 0$ . Thus skyrmions can be generated in rotating and interacting two-component BECs without SOC. The detailed

discussion can be found in related literature.<sup>45,61</sup> As mentioned above, the skyrmion with fixed unit topological charge  $|Q| = 1$  can display different configurations. As pointed out in Ref.,<sup>41</sup> the hyperbolic-radial(out) skyrmion, hyperbolic-radial(in) skyrmion, and circular-hyperbolic skyrmion have two extreme values of  $S_z$ : a minima and a maximum. The radial-in skyrmion, radial-out skyrmion, circular skyrmion, and hyperbolic skyrmion can be distinguished by using three characteristic numbers: polarity  $p = \text{sgn}[\mathbf{e}_z \cdot \mathbf{S}(r = 0)]$ , circulation  $c = \text{sgn}\{\mathbf{e}_z \cdot [\mathbf{r} \times \mathbf{S}(r \neq 0)]\}$ , and divergence  $d = \text{sgn}[\mathbf{e}_r \cdot \mathbf{S}(r \neq 0)]$ .<sup>62</sup> In the following sections, one can see that the other parameters, such as the SOC, also significantly influence the structure of formed skyrmions (see Figs. 2, 6 and 8). As a matter of fact, the components of spin density  $S_x$ ,  $S_y$ , and  $S_z$  depend on the component wave functions  $\psi_{1,2}$  and the corresponding complex conjugates  $\psi_{1,2}^*$  of the ground state of the system as shown in Eqs. (7)-(9). Therefore the complex skyrmion structures can be formed in the spin textures for different combinations of parameters.

Note that sometimes the hyperbolic-radial(out) skyrmion, hyperbolic-radial(in) skyrmion and circular-hyperbolic skyrmion can also be called a pair of merons (half-skyrmions) which is early proposed in the study of superfluid Helium with particular cylindrical boundary conditions<sup>63</sup> and is associated with the so-called Mermin-Ho vortices.<sup>64</sup> The topological charges of a meron (half-skyrmion) and an anti-meron (half-antiskyrmion) are  $1/2$  and  $-1/2$ , respectively. Recent investigation shows that not all cases of the above three types of skyrmions can be regarded as meron pairs.<sup>41</sup> For the meron pair, the topological charge density is distributed anisotropically along the polarization direction of the meron pair, and there is a configuration of vortex-antivortex pair in the relative phase distribution of the two (pseudo)spin components, where the two vortices are connected by a domain wall with fixed phase difference of  $2\pi$ .<sup>45,61</sup> In addition, the spin vector for a meron (half-skyrmion) covers a half of a unit sphere of spin space while that for a skyrmion sweeps the whole unit sphere of spin space, which is due to the fact that their topological charges are  $1/2$  and  $1$ , respectively. In other words, for a certain unit cell, a skyrmion means that if the spin-density components  $S_x$  and  $S_y$  can vary from  $-1$  to  $1$ , then the spin-density component  $S_z$  also varies from  $-1$  to  $1$ . By comparison, a meron (half skyrmion) implies that the spin-density component  $S_z$  just varies from  $-1$  to  $0$  or from  $0$  to  $1$ . In our numerical calculations we identify skyrmions and merons (half skyrmions) by combining density distribution, phase distribution, relative phase distribution (when necessary), spin texture, three spin-density components, topological charge density, local topological charge in a certain unit cell, and the above features of skyrmions and merons (half skyrmions).

### 3.2 Combined effect of SOC, rotation and interatomic interactions

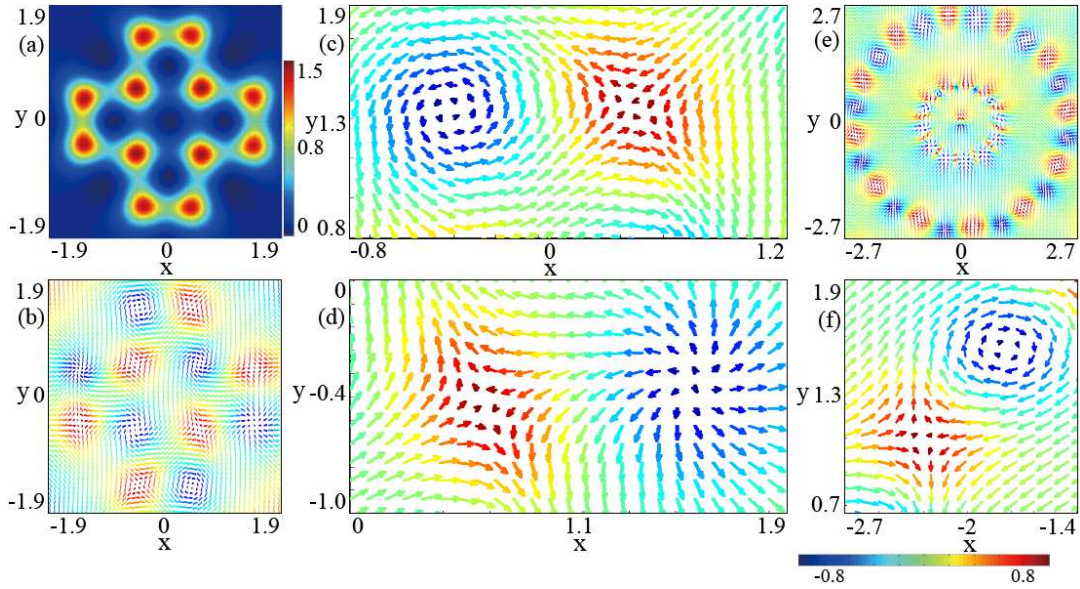
#### 3.2.1 Fixed isotropic D-SOC

Figure 3 shows the density distributions (the left two columns) and phase distributions (the right two columns) for the ground states of rotating anharmonic spin-1/2 BECs with relatively small isotropic D-SOC,  $\lambda_x = \lambda_y = 1$ , where the odd and even columns denote component 1 and component 2, re-

spectively. The rotation frequencies for the initial component mixing with  $\delta = 0.5$  in rows (a) and (b) are  $\Omega = 0.5$  and  $\Omega = 3$ , and those for the component separation with  $\delta = 2$  in rows (c)-(f) are  $\Omega = 0.2$ ,  $\Omega = 0.6$ ,  $\Omega = 2$  and  $\Omega = 3$ , respectively. For the initially miscible BECs, when the rotation frequency is small there is a visible vortex in the center of component 1 and there are two visible vortices in component 2, where the three vortices alternatively arrange into a straight line (see Fig. 3(a)). When the rotation frequency increases to  $\Omega = 3$ , each component generates a complex topological structure composed of an annular visible vortex lattice (i.e., a visible vortex necklace) and a large density hole. Here the large density hole denotes a hidden giant vortex plus a hidden annular vortex lattice (hidden vortex necklace) rather than a pure giant vortex predicted in rotating conventional BECs<sup>37</sup> or rotating Rashba spin-orbit coupled BECs in a harmonic trap.<sup>31-34</sup> Furthermore, the density profiles and phase profiles for the two components become similar except that there is a hidden giant vortex with six circulation quanta in the center of component 1 while one with seven circulation quanta in the center of component 2. Although giant vortices are not easy to be observed in rotating conventional BECs due to their instability,<sup>65</sup> our present results indicate that they can be easily detected in rotating spin-orbit coupled BECs in the anharmonic trap. Thus the topological structure of the system is strongly affected by the interplay among the SOC, rotation frequency, the interatomic interactions, and the anharmonic trap.

For the initially immiscible BECs, when the rotation frequency is small, e.g.,  $\Omega = 0.2$  and  $\Omega = 0.6$ , the two components exhibit obvious phase separation as shown in Figs. 3(c) and 3(d). The topological structures of the system in Figs. 3(c) and 3(d) are typical Anderson-Toulouse coreless vortices<sup>66</sup> (some recent literature also called them half-quantum vortices<sup>13,32</sup>), where the core of the circulating external component is filled with the other nonrotating component. With the further increase of rotation frequency, component 1 evolves into a special topological configuration which is composed of an exterior vortex necklace and a hidden triangular vortex lattice in the central and very narrow region, while component 2 develops into a topological structure comprised of an outer annular vortex lattice and an inner square vortex lattice (see Fig. 3(e)). Here the two components still keep good phase separation, and the topological defects essentially form alternative circular vortex sheets. When the rotation frequency increases to  $\Omega = 3$ , the visible vortices in each component form an annular vortex lattice, which is similar to the case of initial phase mixing. The region of the large density hole is occupied by a central hidden giant vortex (a doubly quantized vortex for component 1 and a triply quantized vortex for component 2) and a hidden vortex necklace. Therefore one can conclude that when the rotation is relatively small the topological defects of the ground state are jointly determined by the interatomic interactions, SOC, rotation frequency, and anharmonic confinement. When  $\Omega$  is large enough, however, rotation plays a crucial role in the topological defect formation of the system.

Displayed in Figs. 4(a) and 4(c) are the topological charge densities for the parameters in Figs. 3(a) and 3(d), respectively. The corresponding spin textures are shown in Figs. 4(b) and 4(d). The spin texture in Fig. 4(b) represents a special topological structure with topological charge approach-



**Fig. 2.** (Color online) Topological charge density and spin textures of spin-1/2 BECs without SOC in a rotating anharmonic trap, where  $\lambda_x = \lambda_y = 0$ , and  $\delta = 0.5$ . (a) Topological charge density for  $\Omega = 1.65$ , (b) the corresponding spin texture, and (c)-(d) local enlargement of the spin texture, where the ground state is given in Fig. 1(b). (e) Spin texture for  $\Omega = 3$  and (f) local enlargement of the spin texture, where the ground state is shown in Fig. 1(d). The color of each arrow indicates the magnitude of  $S_z$ . The horizontal and vertical coordinates  $x$  and  $y$  are in units of  $a_0$ .

ing  $Q = 3/2$  which is comprised of a radial-out meron in the center and two symmetric hyperbolic merons in the two sides. The exotic spin defect may be called a meron cluster consisting of three merons. Shown in Fig. 4(d) is a typical hyperbolic skyrmion with unit topological charge  $Q = 1$  whose ground-state structure generally corresponds to an Anderson-Toulouse coreless vortex.

### 3.2.2 Fixed rotation frequency

Our calculations show that in the absence of rotation the large SOC strengths favor vortex chains for initially mixed BECs and stripe phases as well as heliciform-stripe phases for initially demixed BECs. For relatively small rotation frequency  $\Omega < 1$ , the ground states of the system are somewhat similar to those of spin-orbit coupled BECs in a rotating harmonic trap.<sup>31,32,34</sup> For the sake of brevity, we will not repeat these results in this work. Here we mainly focus on the case of large rotation frequency, i.e.  $\Omega > 1$ . Figure 5 shows the density distributions and phase distributions of the system with fixed rotation frequency  $\Omega = 1.2$  above the radial trapping frequency, which is usually not accessible in conventional rotating BECs confined in a harmonic trap.<sup>31-35,41,49</sup> The columns from left to right represent  $|\psi_1|^2$ ,  $|\psi_2|^2$ ,  $\arg\psi_1$ , and  $\arg\psi_2$ , respectively. Here the strengths of the 2D isotropic D-SOC for the initial component mixing with  $\delta = 0.5$  in rows (a)-(c) and those for the initial component separation with  $\delta = 2$  in rows (d) and (e) are  $\lambda_x = \lambda_y = 0.8$  and  $\lambda_x = \lambda_y = 25$ , respectively. In the case of initial component mixing and weak D-SOC, four visible vortices arrange into a square vortex lattice in component 1, while in component 2 the five visible vortices constitute a criss-cross vortex string, which reduces effectively the energy of system to the minimum (see Fig. 5(a)). Essentially, the visible vortices in the system form a coreless vortex lattice as a whole because the vortices are alternatively distributed in the two components and the remainder of the two components keep mixing, which means that there is no

topological defect in the total density distribution. With the increase of D-SOC strength, e.g.,  $\lambda_x = \lambda_y = 2$ , there exists a topological phase transition for the vortex structure of the system. From Fig. 5(b), the vortex number in each component increases evidently because the stronger SOC means the larger orbital angular momentum input into the system. In addition, the vortices in each component form an annular vortex lattice plus a central vortex (a singly-quantized central vortex for component 1 while a doubly-quantized central vortex for component 2). As a result, the visible vortices compose a nucleated vortex lattice which is remarkably different from Fig. 5(a) because there are evident vortex defects in the total density distribution of the system.

For a strong D-SOC with  $\lambda_x = \lambda_y = 25$ , there is an almost full overlap of the density distributions and the phase distributions between the two components. This character occurs for not only the case of initial phase mixing but also the case of initial phase separation (see Figs. 5(c) and 5(e)). Here the visible vortices constitute multilayer ringlike structures. Our simulation shows that the region of the large density hole is occupied by a central hidden giant vortex and several hidden vortex necklaces (see Figs. 5(c) and 5(e)), which is quite different from the conventional prediction results in rotating spin-orbit coupled BECs in a harmonic trap.<sup>31-35</sup> For the latter case, the large density hole in the density distribution at large rotation frequency corresponds to a pure giant vortex. It is shown that the present anharmonic system can exhibit rich and complex topological configuration due to the interplay among interatomic interactions, rotation, SOC, and anharmonic confinement.

In the case of initial component separation and weak D-SOC, the two component densities exhibit obvious phase separation as shown in Fig. 5(d), where the visible vortices or hidden vortices in the two components tend to form annular structures layer by layer. With the further increase of D-SOC, e.g.,  $\lambda_x = \lambda_y = 25$ , more vortices generate in the cloud

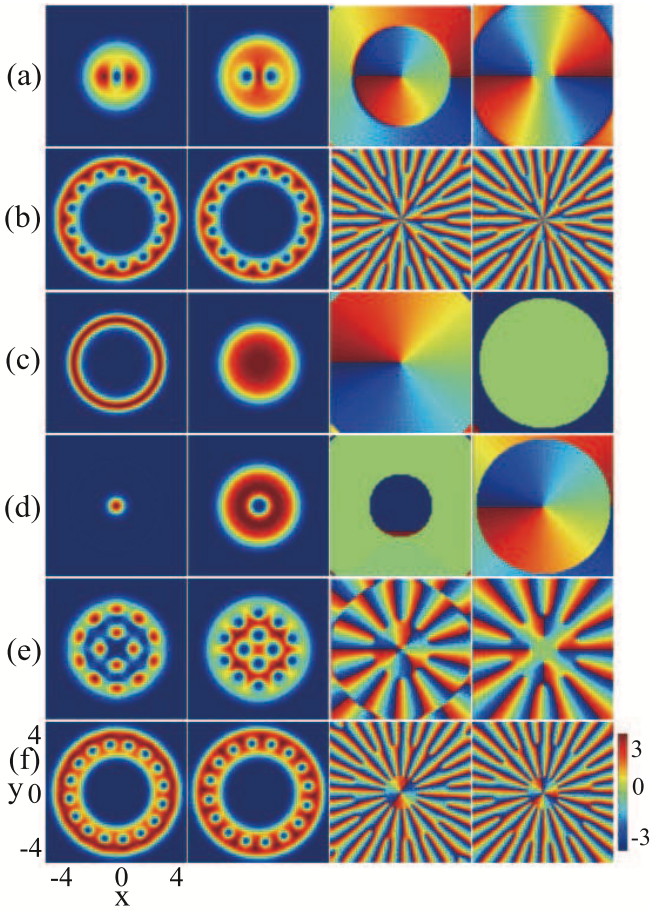


**Fig. 3.** (Color online) Ground-state density distributions and phase distributions for rotating anharmonic spin-1/2 BECs with  $\lambda_x = \lambda_y = 1$ . (a)  $\delta = 0.5$ ,  $\Omega = 0.5$ , (b)  $\delta = 0.5$ ,  $\Omega = 3$ , (c)  $\delta = 2$ ,  $\Omega = 0.2$ , (d)  $\delta = 2$ ,  $\Omega = 0.6$ , (e)  $\delta = 2$ ,  $\Omega = 2$ , and (f)  $\delta = 2$ ,  $\Omega = 3$ . The columns from left to right denote  $|\psi_1|^2$ ,  $|\psi_2|^2$ ,  $\arg\psi_1$ , and  $\arg\psi_2$ , respectively. The horizontal and vertical coordinates  $x$  and  $y$  are in units of  $a_0$ .

and form a rather complex topological structure comprised of three-layer visible vortex necklaces and several hidden vortex necklaces as well as a central hidden giant vortex (see Fig. 5(e)), which is similar to that in Fig. 5(c). Physically, the strong D-SOC or the rapid rotation will result in large kinetic energy. Here the kinetic energy acts against the interspecies interaction. The latter is responsible for component demixing while the former tends to expand the BECs and hence favors component mixing. In the mean time, the anharmonic trapping potential tends to trap the BECs more tightly and thus also sustains component mixing. Thus component separation can be suppressed by the kinetic energy and external potential in some conditions even if the relation  $\beta_{11}\beta_{22} < \beta_{12}^2$  is satisfied, as we can see in Figs. 1, 2 and 5. In addition, we can find that when relevant parameters such as interatomic interactions and rotation frequency are fixed the D-SOC can be used to control the topological structure of the rotating anharmonic BECs.

The topological charge density and the spin texture for the parameters in Fig. 5(a) are demonstrated in Fig. 6. From Fig. 6(a), the topological charge density exhibits a petal-like structure composed of four evident criss-cross petals and an inconspicuous torus in the trap center. Figure 6(b) is the corresponding spin texture, where the local amplifications are

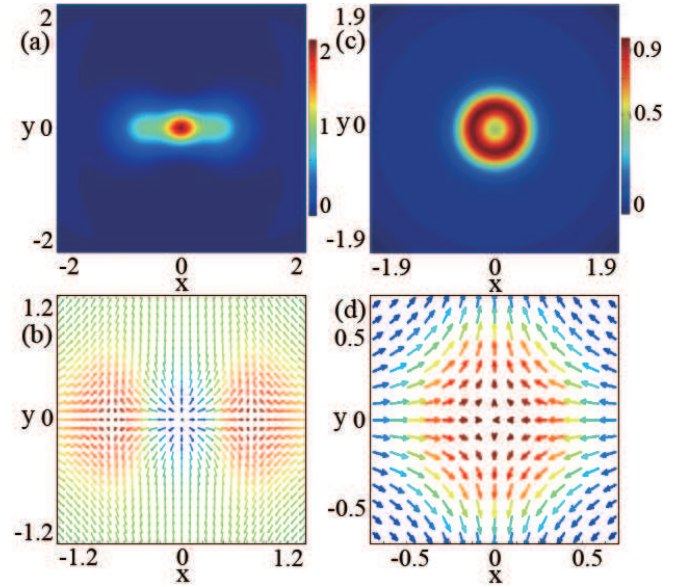


**Fig. 4.** (Color online) Topological charge densities (a), (c) and spin textures (b), (d) for the ground states of interacting spin-1/2 BECs in a rotating anharmonic trap, where  $\lambda_x = \lambda_y = 1$ . (a)-(b)  $\delta = 0.5$ ,  $\Omega = 0.5$ , (c)-(d)  $\delta = 2$ ,  $\Omega = 0.6$ . The horizontal and vertical coordinates  $x$  and  $y$  are in units of  $a_0$ .

displayed in Figs. 6(c) and 6(d). The four skyrmions and one half-skyrmion (meron) in Fig. 6(b) constitute a novel skyrmion lattice in which the vertical two spin defects are hyperbolic-radial(in) skyrmions, the horizontal two spin defects are hyperbolic-radial(out) skyrmions, and the central spin defect is a hyperbolic half-skyrmion (meron).<sup>40,41,45</sup> Our nonlinear stability analysis shows that the vortex structures, skyrmion structures and topological properties of the system are rather stable when the SOC strength or the rotation frequency is not too large. In addition, we find that as the SOC strength or rotation frequency increases the topological charge of the system is increases first and then decreases. For very strong D-SOC or very fast rotation, however, the skyrmion lattice configuration in spin textures will be destroyed. Physically, when the SOC strength (with fixed rotation frequency) or the rotation frequency (with fixed SOC) increases, more angular momentum contributes to the system and leads to generation of more vortices, regardless of the initial state of the system being mixed or separated. In this case most vortices in component 1 and those in component 2 are separated from each in space due to the repulsive interspecies interaction, which means that the total topological charge of the system continues to increase. However, when the SOC strength or the rotation frequency become very large the system favors an almost full overlap between the densities of the two components because higher angular momentum states become dominant as seen in Figs. 1, 3 and 5, which indicates the topological density  $q(\mathbf{r})$  decreases remarkably due to  $S_z \rightarrow 0$ . According to Equation (10), it is easy to prove that the topological charge density is strictly zero for any planar spin texture. Thus the total topological charge decreases dramatically for the case of very large SOC strength or rotation frequency.

### 3.3 Effects of anisotropic D-SOC and RD-SOC

Next, we consider the ground-state properties of rotating anharmonic BECs with anisotropic D-SOC and those with

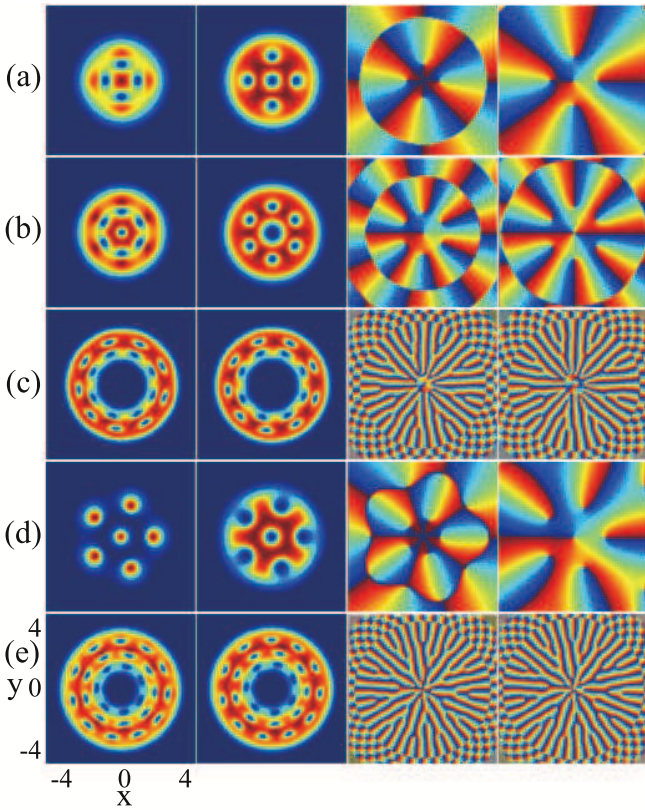


**Fig. 5.** (Color online) Ground states of rotating interacting spin-1/2 BECs with D-SOC in an anharmonic trap, where  $\Omega = 1.2$ . (a)  $\delta = 0.5$ ,  $\lambda_x = \lambda_y = 0.8$ , (b)  $\delta = 0.5$ ,  $\lambda_x = \lambda_y = 2$ , (c)  $\delta = 0.5$ ,  $\lambda_x = \lambda_y = 25$ , (d)  $\delta = 2$ ,  $\lambda_x = \lambda_y = 0.8$ , and (e)  $\delta = 2$ ,  $\lambda_x = \lambda_y = 25$ . The columns from left to right denote  $|\psi_1|^2$ ,  $|\psi_2|^2$ ,  $\arg\psi_1$  and  $\arg\psi_2$ , respectively. The horizontal and vertical coordinates  $x$  and  $y$  are in units of  $a_0$ .

anisotropic RD-SOC. The D-SOC and RD-SOC can be realized within current experimental techniques,<sup>1-4,7-9,19,43,44</sup> and we will also discuss the difference between the D-SOC effect and the RD-SOC effect. In the isotropic case of  $\lambda_x = \lambda_y$ , the RD-SOC belongs to the R-SOC type, so we may only consider the anisotropic case. Figure 7 shows the density distributions (the left columns of (a)-(f)) and phase distributions (the right columns of (a)-(f)) of component 1 for the ground states of rotating anharmonic spin-1/2 BECs with anisotropic D-SOC or RD-SOC. Note that Figs. 7(a), 7(b), 7(d) and 7(e) denote the cases of D-SOC and the others represent the cases of RD-SOC.

In the case of  $\Omega = 0.9$ , for 1D D-SOC there is an obvious vortex chain along the  $x = 0$  axis because of the 1D spin-orbit interaction along the  $y$  direction as shown in Fig. 7(a). The density distribution exhibits well symmetry with respect to the  $x = 0$  axis and the  $y = 0$  axis. Component 2 has similar density distribution and phase distribution except that the vortices in the two components are staggered in space, which is not shown here for the sake of simplicity. When  $\lambda_y$  is enhanced, only the number of vortices along the  $x = 0$  axis increases without changing the symmetry of the density distribution. For 2D anisotropic D-SOC, there is no density symmetry with respect to the  $x = 0$  axis or the  $y = 0$  axis (see Fig. 7(b)). By comparison, for the case of anisotropic RD-SOC, the system keeps well the symmetry with respect to  $x = 0$  axis and  $y = 0$  axis, especially for the latter case and for the exte-

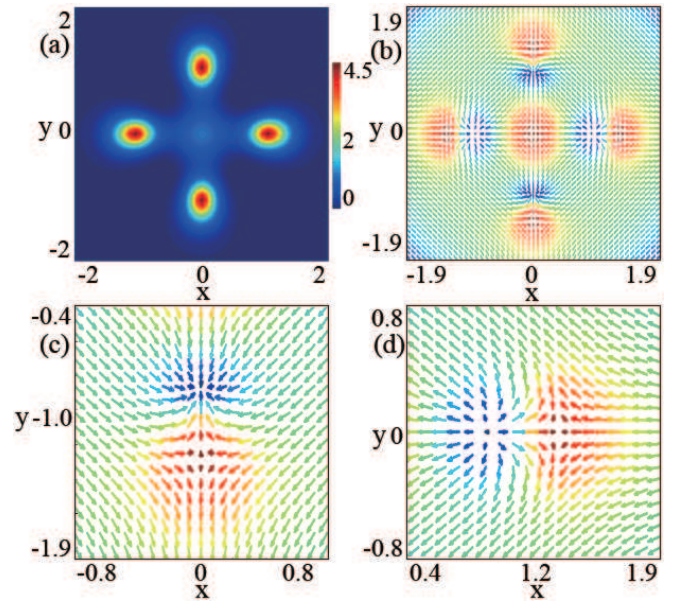


**Fig. 6.** (Color online) Topological charge density (a) and spin textures (b)-(d), where  $\delta = 0.5$ ,  $\lambda_x = \lambda_y = 0.8$ , and  $\Omega = 1.2$ . The corresponding ground state is shown in Fig. 5(a). (c) and (d) are the local amplifications of the spin texture. The horizontal and vertical coordinates  $x$  and  $y$  are in units of  $a_0$ .

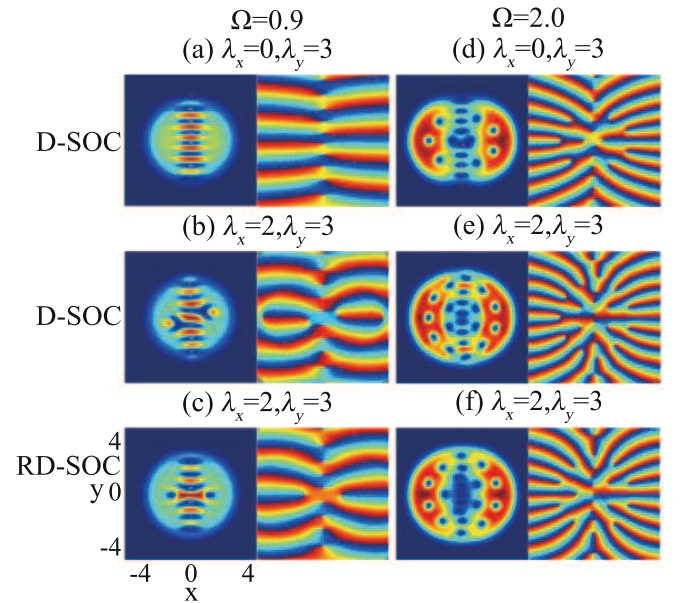


**Fig. 7.** (Color online) Density distributions  $|\psi_1|^2$  (the left columns of (a)-(f)) and phase distributions  $\arg\psi_1$  (the right columns of (a)-(f)) for the ground states of rotating anharmonic spin-1/2 BECs with anisotropic D-SOC and those with anisotropic RD-SOC, where  $\delta = 2.0$ . (a), (b), (d) and (e) are the cases of anisotropic D-SOC, while (c) and (f) are the cases of anisotropic RD-SOC. (a)  $\Omega = 0.9$ ,  $\lambda_x = 0$ ,  $\lambda_y = 3$ , (b)-(c)  $\Omega = 0.9$ ,  $\lambda_x = 2$ ,  $\lambda_y = 3$ , (d)  $\Omega = 2.0$ ,  $\lambda_x = 0$ ,  $\lambda_y = 3$ , and (e)-(f)  $\Omega = 2.0$ ,  $\lambda_x = 2$ ,  $\lambda_y = 3$ . The horizontal and vertical coordinates  $x$  and  $y$  are in units of  $a_0$ .

rior region in the density distribution (see Figs. 7(c) and 7(f)). Similar properties also exist for large rotation frequency, e.g.,  $\Omega = 2$ . In Fig. 7(d), vortices are distributed not only along the  $y$  direction but also along the  $x$  direction, where the symmetry with respect to  $x = 0$  axis is broken while the symmetry with respect to  $y = 0$  axis are basically unchanged. The physical mechanism is that for large rotation frequency the  $x$ -direction

vortex chain caused by the combined effect of 1D D-SOC and rotation can only carry finite angular momentum and the residual angular momentum is inevitably carried by the transverse vortices beside the  $x = 0$  axis. For 2D anisotropic D-SOC with  $\lambda_x = 2$  and  $\lambda_y = 3$ , more vortices are generated in the system and there is a distorted vortex chain along the  $y$  direction, but both the density symmetry concerning the  $x = 0$  axis and that concerning the  $y = 0$  axis are destroyed, where the outer vortices tend to form an annular vortex array (Fig. 7(e)). The main reason is that the kinetic energy plays a key role in the ground-state structure of the system for large rotation frequency. When the SOC is Rashba-Dresselhaus type (see Fig. 7(f)), the density distribution restores the excellent symmetry concerning the  $y = 0$  axis, which is similar to Fig. 7(c).

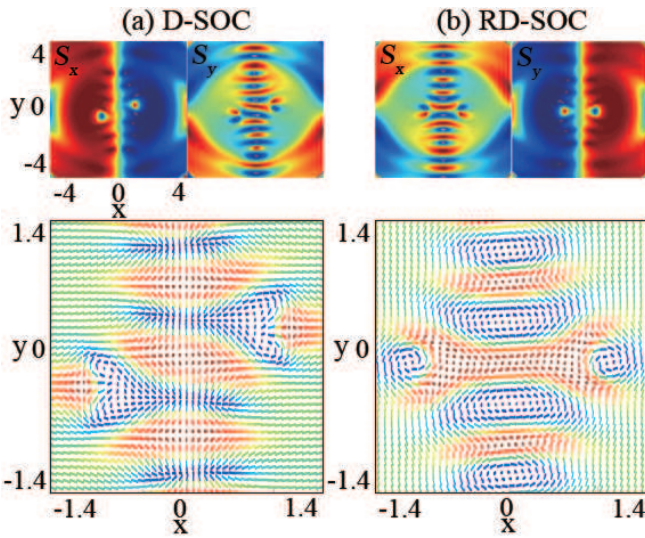


**Fig. 8.** (Color online) The components  $S_x$  and  $S_y$  (the top row) of spin density vector and the spin textures (the bottom row), where  $\delta = 2.0$ ,  $\Omega = 0.9$ ,  $\lambda_x = 2$ , and  $\lambda_y = 3$ . (a) and (b) denote the case of anisotropic D-SOC and that of anisotropic RD-SOC, respectively. The horizontal and vertical coordinates  $x$  and  $y$  are in units of  $a_0$ .

The  $S_x$  and  $S_y$  components of spin density vector and the corresponding spin textures for the parameters in Figs. 7(b) and 7(c) are displayed in Fig. 8. In the pseudo-spin representation, the blue region denotes spin-down and the red region denotes spin-up. In the case of D-SOC,  $S_x$  and  $S_y$  obey neither even nor odd parity distribution along the  $x$  direction or the  $y$  direction (Fig. 8(a)). By comparison, in the case of RD-SOC,  $S_x$  satisfies the even parity distribution along the  $x$  direction and the odd parity distribution along the  $y$  direction, while it is just the reverse for  $S_y$  (Fig. 8(b)). At the same time, the spin component  $S_x$  ( $S_y$ ) in Fig. 8(a) (Fig. 8(b)) forms two remarkable spin domains, and the boundary between the two spin domain develops into a domain wall with  $|S_x| \neq 1$  ( $|S_y| \neq 1$ ). Generally, the spin domain wall for nonrotating two-component BECs is a classical Néel wall, where the spin flips only along the vertical direction of the wall. However, our numerical simulation of the spin texture shows that in the region of spin domain wall the spin flips not only along the  $x$  direction (the vertical direction of domain wall) but also along the  $y$  direction (the domain-wall direction), which

indicates that the observed spin domain wall in the present system is a new type of domain wall. Here the anisotropic SOC leads to the creation of more interesting and complicated skyrmion structures. This feature is present evidently for both the cases of anisotropic D-SOC and anisotropic RD-SOC. For the case of D-SOC, there is an obvious radial(in) skyrmion string along the  $x = 0$  axis with two asymmetric hyperbolic skyrmions standing on either side of the axis. By comparison, a circular skyrmion string is distributed along the  $x = 0$  axis with two symmetric circular skyrmions lying on either side of the axis. Note that the ground-state structures and spin textures for the case of anisotropic SOC have not been discussed in the previous investigations on rotating spin-orbit coupled quantum gases.<sup>31–35</sup> We expect that the interesting topological defects and spin textures found in the present work allow to be demonstrated in the future experiments.

#### 4. Conclusion

We have studied the ground-state structures of interacting two-component BECs with D-SOC or RD-SOC in a rotating anharmonic trap. The effects of rotation, SOC, interatomic interaction, and trap anharmonicity on the ground-state structure of this system are analyzed and discussed systematically. In the absence of SOC, with the increase of rotation frequency the system experiences structural phase transitions from singly quantized vortex state to square vortex lattice, square vortex lattice to triangular vortex lattice, and triangular vortex lattice to ringlike vortex lattice. In the presence of isotropic D-SOC, the system supports vortex pair, Anderson–Toulouse coreless vortices, circular vortex sheets and combined complex topological structures comprised of a visible vortex necklace and a central hidden giant vortex plus a hidden vortex necklace, where the latter does not depend on the interaction parameters. In addition, large D-SOC yields a visible multi-layer vortex necklace and a central hidden giant vortex as well as several hidden vortex necklaces. Furthermore, it is shown that the system sustains single basic skyrmion, meron cluster, skyrmion string and various complex skyrmion lattices including criss-cross skyrmion lattices and multi-ring skyrmion lattices. In the limit of large SOC or rotation frequency, the skyrmion configurations in spin textures will be destroyed due to the enhanced overlap between the two component densities and thus the distinct reduction of topological charge density. Moreover, the effects of anisotropic D-SOC and RD-SOC on the topological structures of the system are discussed. Compared with the case of anisotropic D-SOC, the system for the case of anisotropic RD-SOC maintains well the symmetry with respect to  $x = 0$  and  $y = 0$  axes, especially for the latter case and for the outer region in the density distribution. New domain wall and skyrmion structures are revealed in the cases of anisotropic SOC. The exotic topological defects and spin textures can be tested and observed in the future experiments, and thus the work presents fantastic perspective for topological excitations in cold atom physics and condensed matter physics.

L.W. thanks Chuanwei Zhang, Hui Zhai, Yongping Zhang, Zhi-Fang Xu, Xiang-Fa Zhou, and Malcolm Jardine for helpful discussions, and acknowledges the research group of Professor W. Vincent Liu at the University of Pittsburgh, where part of the work was carried out. In addition, we give special thanks to Professor Ran Cheng at the University of California,

Riverside for his productive discussions and insightful suggestions. This work is supported by the National Natural Science Foundation of China (Grant No. 11475144), the Natural Science Foundation of Hebei Province of China (Grant No. A2015203037), and Research Foundation of Yanshan University (Grant No. B846).

- 1) Y. -J. Lin, K. Jiménez-García, and I. B. Spielman, *Nature* **471**, 83 (2011).
- 2) L. W. Cheuk, A. T. Sommer, Z. Hadzibabic, T. Yefsah, W. S. Bakr, and M. W. Zwierlein, *Phys. Rev. Lett.* **109**, 095302 (2012).
- 3) Z. M. Meng, L. H. Huang, P. Peng, D. H. Li, L. C. Chen, Y. Xu, C. Zhang, P. Wang, and J. Zhang, *Phys. Rev. Lett.* **117**, 235304 (2016).
- 4) Z. Wu, L. Zhang, W. Sun, X. T. Xu, B. Z. Wang, S. C. Ji, Y. Deng, S. Chen, X. J. Liu, and J. W. Pan, *Science* **354**, 83 (2016).
- 5) D. Xiao, M. C. Chang, and Q. Niu, *Rev. Mod. Phys.* **82**, 1959 (2010).
- 6) X. Li, W. V. Liu, and L. Balents, *Phys. Rev. Lett.* **112**, 067202 (2014).
- 7) L. Huang, Z. Meng, P. Wang, P. Peng, S. L. Zhang, L. Chen, D. Li, Q. Zhou, and J. Zhang, *Nat. Phys.* **12**, 540 (2016).
- 8) S. Kolkowitz, S. L. Bromley, T. Bothwell, M. L. Wall, G. E. Marti, A. P. Koller, X. Zhang, A. M. Rey, and J. Ye, *Nature* **542**, 66 (2017).
- 9) J. R. Li, J. Lee, W. Huang, S. Burchesky, B. Shteynas, F. C. Top, A. O. Jamison, and W. Ketterle, *Nature* **543**, 91 (2017).
- 10) C. Wang, C. Gao, C. M. Jian, and H. Zhai, *Phys. Rev. Lett.* **105**, 160403 (2010).
- 11) S. Sinha, R. Nath, and L. Santos, *Phys. Rev. Lett.* **107**, 270401 (2011).
- 12) H. Hu, B. Ramachandhran, H. Pu, and X. J. Liu, *Phys. Rev. Lett.* **108**, 010402 (2012).
- 13) B. Ramachandhran, B. Opanchuk, X. J. Liu, H. Pu, P. D. Drummond, and H. Hu, *Phys. Rev. A* **85**, 023606 (2012).
- 14) T. Kawakami, T. Mizushima, M. Nitta, and K. Machida, *Phys. Rev. Lett.* **109**, 015301 (2012).
- 15) Y. Zhang, L. Mao, and C. Zhang, *Phys. Rev. Lett.* **108**, 035302 (2012).
- 16) Q. Zhu, C. Zhang, and B. Wu, *Europhys. Lett.* **100**, 50003 (2012).
- 17) Y. Xu and C. Zhang, *Phys. Rev. Lett.* **114**, 110401 (2015).
- 18) A. C. White, Y. Zhang, and T. Busch, *Phys. Rev. A* **95**, 041604 (2017).
- 19) C. Qu, C. Hamner, M. Gong, C. Zhang, and P. Engels, *Phys. Rev. A* **88**, 021604(R) (2013).
- 20) H. Sakaguchi and K. Umeda, *J. Phys. Soc. Jpn.* **85**, 064402 (2016).
- 21) H. Sakaguchi and B. A. Malomed, *Phys. Rev. A* **96**, 043620 (2017).
- 22) S. Stringari, *Phys. Rev. Lett.* **118**, 145302 (2017).
- 23) M. A. Khamehchi, K. Hossain, M. E. Mossman, Y. Zhang, T. Busch, M. M. Forbes, and P. Engels, *Phys. Rev. Lett.* **118**, 155301 (2017).
- 24) Y. V. Kartashov and V. V. Konotop, *Phys. Rev. Lett.* **118**, 190401 (2017).
- 25) R. Sakamoto, Y. Ono, R. Hatsuda, K. Shiina, E. Arahata, and H. Mori, *J. Phys. Soc. Jpn.* **86**, 075003 (2017).
- 26) Y. Xu, Y. Zhang, and B. Wu, *Phys. Rev. A* **87**, 013614 (2013).
- 27) S. Gautam and S. K. Adhikari, *Phys. Rev. A* **97**, 013629 (2018).
- 28) V. Achilleos, J. Stockhofe, P. G. Kevrekidis, D. J. Frantzeskakis, and P. Schmelcher, *Europhys. Lett.* **103**, 20002 (2013).
- 29) Y. Xu, L. Mao, B. Wu, and C. Zhang, *Phys. Rev. Lett.* **113**, 130404 (2014).
- 30) Y. Zhang, Y. Xu, and T. Busch, *Phys. Rev. A* **91**, 043629 (2015).
- 31) X. Q. Xu and J. H. Han, *Phys. Rev. Lett.* **107**, 200401 (2011).
- 32) X. F. Zhou, J. Zhou, and C. Wu, *Phys. Rev. A* **84**, 063624 (2011).
- 33) J. Radić, T. A. Sedrakyan, I. B. Spielman, and V. Galitski, *Phys. Rev. A* **84**, 063604 (2011).
- 34) A. Aftalion and P. Mason, *Phys. Rev. A* **88**, 023610 (2013).
- 35) A. L. Fetter, *Phys. Rev. A* **89**, 023629 (2014).
- 36) Z. F. Xu, S. Kobayashi, and M. Ueda, *Phys. Rev. A* **88**, 013621 (2013).
- 37) A. L. Fetter, B. Jackson, and S. Stringari, *Phys. Rev. A* **71**, 013605 (2005).
- 38) G. Dresselhaus, *Phys. Rev.* **100**, 580 (1955).
- 39) N. Goldman, G. Juzeliūnas, P. Öhberg, and I. B. Spielman, *Rep. Prog. Phys.* **77**, 126401 (2014).
- 40) T. H. R. Skyrme, *Nucl. Phys.* **31**, 556 (1962).
- 41) C. F. Liu, H. Fan, Y. C. Zhang, D. S. Wang, and W. M. Liu, *Phys. Rev. A* **86**, 053616 (2012).
- 42) H. Zhai, W. Q. Chen, Z. Xu, and L. Chang, *Phys. Rev. A* **68**, 043602 (2003).
- 43) T. Ozawa and G. Baym, *Phys. Rev. A* **85**, 013612 (2012).
- 44) W. Han, G. Juzeliūnas, W. Zhang, and W. M. Liu, *Phys. Rev. A* **91**, 013607 (2015).
- 45) K. Kasamatsu, M. Tsubota, and M. Ueda, *Phys. Rev. Lett.* **93**, 250406 (2004).
- 46) L. H. Wen, Y. Qiao, Y. Xu, and L. Mao, *Phys. Rev. A* **87**, 033604 (2013).
- 47) B. Wu and Q. Niu, *New J. Phys.* **5**, 104 (2003).
- 48) L. H. Wen and J. H. Li, *Phys. Rev. A* **90**, 053621 (2014).
- 49) K. Kasamatsu, M. Tsubota, and M. Ueda, *Phys. Rev. Lett.* **91**, 150406 (2003).
- 50) P. Mason and A. Aftalion, *Phys. Rev. A* **84**, 033611 (2011).
- 51) L. H. Wen, H. W. Xiong, and B. Wu, *Phys. Rev. A* **82**, 053627 (2010).
- 52) L. H. Wen and X. B. Luo, *Laser Phys. Lett.* **9**, 618 (2012).
- 53) T. Mithun, K. Porsezian, and B. Dey, *Phys. Rev. A* **89**, 053625 (2014).
- 54) R. M. Price, D. Trypogeorgos, D. L. Campbell, A. Putra, A. Valdés-Curiel, and I. B. Spielman, *New J. Phys.* **18**, 113009 (2016).
- 55) A. Schmeller, J. R. Eisenstein, L. N. Pfeiffer, and K. W. West, *Phys. Rev. Lett.* **75**, 4290 (1995).
- 56) D. C. Wright and N. D. Mermin, *Rev. Mod. Phys.* **61**, 385 (1989).
- 57) A. Qaiumzadeh, I. A. Ado, R. A. Duine, M. Titov, and A. Brataas, *Phys. Rev. Lett.* **120**, 197202 (2018).
- 58) H. Ninomiya, S. Nakamura, Y. Kono, S. Kittaka, T. Sakakibara, K. Inoue, and S. Ohara, *J. Phys. Soc. Jpn.* **86**, 124704 (2017).
- 59) I. Kézsmárki, S. Bordács, P. Milde, et al., *Nat. Mater.* **14**, 111 (2015).
- 60) A. S. Ahmed, B. D. Esser, J. Rowland, D. W. McComb, and R. K. Kawakami, *J. Cryst. Growth.* **467**, 38 (2017).
- 61) K. Kasamatsu, M. Tsubota, and M. Ueda, *Phys. Rev. A* **71**, 043611 (2005).
- 62) S. Wintz, C. Bunce, A. Neudert, et al., *Phys. Rev. Lett.* **110**, 177201 (2013).
- 63) G. E. Volovik, *The Universe in a Helium Droplet* (Oxford University Press, Oxford, 2003), Chap. 16.
- 64) N. D. Mermin and T. L. Ho, *Phys. Rev. Lett.* **36**, 594 (1976).
- 65) A. L. Fetter, *Rev. Mod. Phys.* **81**, 647 (2009).
- 66) P. W. Anderson and G. Toulouse, *Phys. Rev. Lett.* **38**, 508 (1977).